RSC Advances

PAPER

View Article Online
View Journal | View Issue

Cite this: *RSC Adv.*, 2026, **16**, 13032

A large-scale and flexible SERS substrate based on sliver decorated nano-cone arrays and its applications for pesticide residue detection

Jie Chen,[a] Mengjie Hu,[a] Tianyuan Liu,[b] Meizhen Huang,[c] Lili Kong,*[d] Xinna Yu*[e] and Qifang Sun*[a]

This paper demonstrates a large-scale, flexible SERS substrate (Ag@R-SERS substrate) based on silver-decorated nano-cone arrays. The substrate was fabricated *via* a two-step process: pre-designed nano-cone arrays were replicated over a large area with high structural uniformity using roll-to-roll ultraviolet nanoimprint lithography (R2R UV-NIL); subsequently, silver nanoparticles (Ag NPs) were self-assembled onto the nano-cone arrays. The performances of the Ag@R-SERS substrate were evaluated using rhodamine 6G (R6G) as a probe molecule with a portable Raman spectrometer. The enhancement factor (EF) and limit of detection (LOD) of R6G detected on Ag@R-SERS substrate were determined to be 5.9×10^7 and 2.65×10^{-8} M. The relative standard deviations (RSDs) of R6G Raman intensities at 1513 cm^{-1} were 5.6% within a single substrate and 6.7% among different substrates. No obvious changes were observed in the line curve of R6G detected by the SERS substrate stored for 20 days. These results demonstrated satisfactory sensitivity, uniformity, reproducibility and stability. Numerical simulations were established to illustrate the electromagnetic enhancement effects of the Ag@R-SERS substrates, which were jointly attributed to the strong coupling effects of densely distributed AgNPs and Ag clusters at the tips of nano-cones. Furthermore, the potential application of the Ag@R-SERS substrate in pesticide detection was explored. Linear relationships between the SERS intensity at 1386 cm^{-1} and thiram concentration were established with R^2 of 0.9986, 0.9940, 0.9974 and the LOD of thiram was determined to be 0.46, 0.49 and 0.55 ppm in ethanol, apple juice and tomato juice, respectively. These results confirm the feasibility of the two-step fabrication method for large-scale, flexible Ag@R-SERS substrates and their applicability for rapid and sensitive pesticide residue detection.

Received 6th January 2026
Accepted 15th February 2026

DOI: 10.1039/d6ra00131a

rsc.li/rsc-advances

1. Introduction

Pesticide residues pose severe threats to food security and environmental protection, which might lead to serious health problems, water and soil pollution, *etc.* An effective and efficient detection method is of great importance to meet the urgent demands of rapid screening of pesticide residues. Surface enhanced Raman spectroscopy (SERS) has been regarded as an emerging analytical method in food safety.[1–4] SERS is able to provide abundant information on molecular structures. Compared with traditional methods in pesticide residue analysis, such as high-performance liquid chromatography (HPLC), gas chromatography (GC) and mass spectroscopy, the SERS technique is rapid, non-invasive and time and cost efficient, without complicated pretreatments. Furthermore, the integration of portable Raman spectrometers and lightweight, easy-to-operate SERS substrates enables on-site analysis.[5–8] SERS could remarkably enlarge cross-sections of Raman scattering relying on notable metal nanoparticles (gold, silver, copper, *etc.*), which are attributed to the electromagnetic enhancement effect and chemical enhancement effect. Sol–gel SERS substrates are widely used, benefiting from their high sensitivity and cost-effectiveness, but they suffer from limitations such as poor storage stability and random particle aggregation during sample preparation. Several SERS substrates have been fabricated on rigid supports, such as glass, silicon wafers, and metal films, to structurally immobilize noble metal nanoparticles. However, these rigid substrates are limited by a small effective detection area, time-consuming fabrication processes, and high production costs. In recent years, flexible SERS substrates have drawn considerable attention, benefiting from their cost-effectiveness, suitability for on-site detection,

[a]*College of Information, Mechanical and Electrical Engineering, Shanghai Normal University, Shanghai 200234, China. E-mail: qifangsun@shun.edu.cn*
[b]*School of Electrical Engineering, Shanghai Jiao Tong University, Shanghai 200240, China*
[c]*School of Automation and Intelligent Sensing, Shanghai Jiao Tong University, Shanghai 200240, China*
[d]*School of Mathematics, Physics and Statistics, Shanghai University of Engineering Science, Shanghai 201620, China. E-mail: lilikco@163.com*
[e]*School of Electrical Engineering and Automation, Jiangsu Normal University, Xuzhou, 221116, Jiangsu, China. E-mail: yuxn@jsnu.edu.cn*

capacity for conformal sampling of real samples, and facile functionalization. Extensive efforts have been devoted to the development of flexible SERS substrates. Paper-based SERS substrates were prepared by dipping, spin-coating and self-assembly methods to achieve plasmonic nanoparticles deposition on the paper platforms;[9–15] these substrates have demonstrated broad applicability in pesticide residue analysis, drug screening, and biomedical diagnostics. Compared with traditional paper-based SERS substrates, cellulose nanofiber (CNF) matrices with high porosity and large specific surface area offer abundant stable sites for plasmonic nanoparticle immobilization, thereby exhibiting superior nanoparticle distribution uniformity and enhanced SERS signal intensity.[16–18] Several SERS membranes have been successfully fabricated by means of simple filtration, which effectively utilizes the inherent physical properties of the filter membrane.[5,19,20] Benefiting from their intrinsic large specific surface area, absorption capacity, and filtration performance, cellulose-based SERS substrates demonstrate significant superiority in sensitivity performance, fabrication convenience and cost-effectiveness. Nevertheless, their practical applications are limited by inherent drawbacks such as poor mechanical strength, acid-base tolerance, time-stability. Wang *et al.*[21] developed a polymer composite SERS membrane composed of epoxy resin, plasmonic metal nanoparticles, and cellulose paper, which retains stable functionality across a broad temperature range of −80 to 100 °C and a wide pH window of 1 to 13. Li *et al.*[22] obtained a PET–Au SERS substrate by a template approach. A polyethylene terephthalate (PET) substrate spin-coated with UV-curable adhesive was bonded to the silicon template patterned with circular nanohole arrays, followed by UV curing, peeling-off, and sequential deposition of a thin chromium (Cr) layer and an 80 nm gold (Au) film. Although the polymer-based SERS substrates exhibited satisfactory stability and excellent solvent/mechanical tolerance, repeatability, fabrication cost, and processing efficiency remained challenges.

In this work, a simple two-step method is proposed to fabricate large-area, flexible, SERS-active substrate (Ag@R-SERS substrate). A roll-to-roll ultraviolet nanoimprint lithography (R2R UV-NIL) technique was applied to continuously fabricate large-scale (2×2 cm^2) cone-shape arrays on the flexible based substrate (R-substrate). A simple wet chemical method was processed to obtain silver nanoparticles (NPs) with intense localized surfaced plasmon resonances (LSPRs). SERS-sensitive silver nanoparticles were then concentrated and deposited on the R-substrate with the assistances of large specific surface areas and hydrophobicity of well-ordered cone-shape arrays. The sensitivity, uniformity, reproducibility, stability performances of Ag@R-SERS substrate were evaluated by a Raman probe of rhodamine 6G (R6G). The enhancement factor (EF) and limit of detection (LOD) of R6G were determined to quantitatively characterize sensitivity. The morphologies of Ag@R-SERS substrate were characterized by scanning electron microscope (SEM) and atomic force microscope (AFM). To further investigate the sensitivity performance of the Ag@R-SERS substrate with respect to the electromagnetic enhancement mechanism, electric field (*E*-field) distributions of silver nanoparticle in vacuum and those immobilized on PET nanocones were simulated by finite element method (FEM). Meanwhile, the promotional effect of the presence of cone-shape nano-arrays on sensitivity enhancement was also evaluated from the perspective of specific surface area. To further explore the practical potential of the Ag@R-SERS substrate for rapid detection of pesticide residues, thiram was applied as the model analyte for subsequent detection and analysis. The linear correlations between Raman spectral signals and thiram concentrations were investigated in ethanol solutions, apple juice, and orange juice, and the LOD was determined for each matrix. All SERS spectra were recorded using a portable Raman spectrometer (Hx-Spec), which validates the feasibility of Ag@R-SERS substrate for rapid, on-site pesticide residue detection.

2. Materials and methods

2.1 Materials

Commercial UV curing resin was purchased from Kangdexin Composite Material Group Co., Ltd (Zhangjiagang, China). The thickness and average transmittance in ultraviolet radiation of PET is respectively 125 μm and 85%. All chemicals are in analytical grades. Hydroxylamine hydrochloride ($NH_2OH \cdot HCl$), sodium hydroxide (NaOH), and silver nitrate ($AgNO_3$) were purchased from purchased from Sinopharm Chemical Co., Ltd (Beijing, China). Ethanol, rhodamine 6G (R6G), thiram were purchased from Aladdin Chemical Co., Ltd (Shanghai, China). Deionized water (DI water) was purified by a Milli-Q Advantage A10 (Burlington, USA) system. The R6G and thiram powder was respectively diluted by DI water and ethanol with different concentrations. The tomato juice was squeezed from a fresh tomato and a simple filtration is proceeded to remove pulp. The apple juice was purchased in supermarket. The juice samples with different concentrations of thiram were prepared for further use.

2.2 Characterizations

The topography of cone-shape arrays on R-substrate was obtained from an atomic force microscope (NanoNavi E-Sweep, SII, Japan). The morphology of Ag@R-SERS substrate was characterized by a scanning electron microscope (JSM-7800F, JEOL, Japan) and the element analysis was operated by Energy Dispersive Spectrometer (EDS). All the SERS spectrums were obtained from a self-developed portable Raman system Hx-Spec which were mainly composed by a diode laser excitation at the wavelength of 785 nm, a compact grating based dispersive spectrometer and a multifunctional integrated probe for signals deliveries and collections. The laser power focused on the Ag@R-SERS substrate and integration time were adjustable.

2.3 Preparation of Ag@R-SERS substrate

The procedures of Ag@R-SERS substrate preparation are schematically shown in Fig. 1, which is consisted of two steps: cone-shape arrays fabrications by R2R UV-NIL and SERS activated process by silver NPs decorations. The R2R UV-NIL method was reported in our previous work.[23] As shown in Fig. 1(a), an anodic

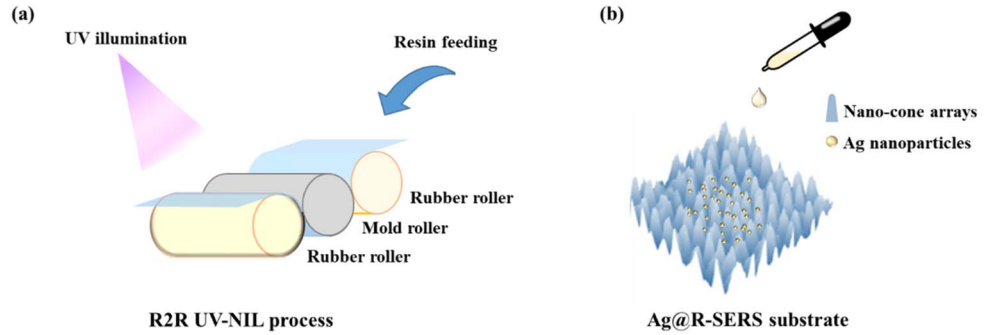

Fig. 1 The schematic diagram of (a) R2R UV-NIL process, (b) Ag@R-SERS substrate activated process by Ag NPs decorations.

aluminum oxide mold (AAO mold, 2 × 2 cm^2) with prepared nanostructures was wrapped on the mold roller and a flexible PET substrate was spread on the rubber rollers. The UV curing resin was injected into the interspace of mold roller and rubber roller. Then the nanostructures could be successfully transferred to the resin-PET substrate due to the pressure effects of rubber rollers and the tension force of PET substrate. A UV light (365 nm, 40 mW cm^{-2}) was irradiated during the R2R process to solidify the UV curing resin.

Nextly, an Ag NPs activated process was carried on to fabricate Ag@R-SERS substrates. A R-substrate was washed with deionized water and alcohol several times to remove impurities. Ag NPs were synthesized by N. Leopold's method.[24] 5.2 mg of $NH_2OH \cdot HCl$ was dissolved in 45 mL of deionized water. 0.3 mL NaOH (1 mol L^{-1}) was added to regulate pH of reaction. $AgNO_3$ aqueous solution (5 mL, 0.1 mol L^{-1}) was rapidly dropped into the $NH_2OH \cdot HCl$–NaOH solution. The mixtures were magnetically stirred for a half hour and then yellow-grey Ag NPs colloids were obtained. Ag NPs colloids were centrifuged at 10 000 rpm for 10 minutes. The supernatant was abandoned and remaining Ag NPs were washed by DI water. The centrifugations were repeated for several times to remove extra chemicals. As demonstrated in Fig. 1(b), 300 μL concentrated Ag NPs aqueous solution was dropped on the R-substrate and dried at 60 °C. Finally, a SERS-active Ag NPs layer was deposited and Ag@R-SERS substrate was obtained.

3. Results and discussion

3.1 Morphology of Ag@R-SERS substrate

The detail parameters of the AAO mold are described as follows. The period of the cone-shape nanostructure (p) is 450 nm, the height (h) is 380 nm, the diameter (d) is 200 nm, and the radius (r) is 50 nm. Fig. 2(a) and (b) demonstrates morphology and line profile of the nano-cone arrays fabricated by R2R UV-NIL, respectively. As shown in Fig. 2(b), the actual heights of cone-shape nanostructures are slightly higher than those of AAO mold, which is due to the pulling effect in the demolding. Fig. 2(c) demonstrates morphology of silver nanoparticles deposited on a silicon wafer. Fig. 2(d) and (e) are top-view SEM images of Ag@R-SERS substrate at different magnifications. As shown in the SEM images, Ag NPs are dispersed and supported on the surface of con-shape nanorods. The supplementary EDS spectrum of Ag@R-SERS substrate is demonstrated in Fig. S1. The most abundant elements are carbon, oxygen and silver. The

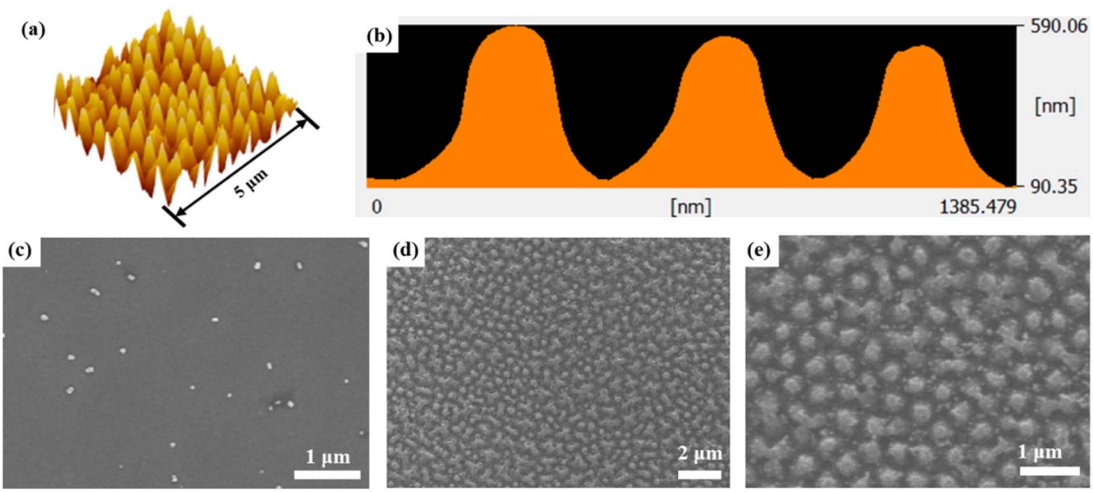

Fig. 2 (a) Morphology and (b) line profile of nano-cone arrays characterised by AFM. (c) SEM of Ag NPs deposited on the silicon wafer. (d and e) SEM images of Ag@R-SERS substrate at different magnifications.

elements of carbon and oxygen are mainly attributed to the PET substrate and UV curing resin. Aside from these elements, a small characteristic peak is observed at 1–1.1 eV, which is most likely attributed to residual sodium from substrate cleaning or reaction processes. Overall, the signals of silver are obviously observed in the EDS result indicating that Ag NPs have been deposited on the cone-shape nanostructures.

3.2 Performances of Ag@R-SERS substrate

3.2.1 Sensitivity characterization and analysis of Ag@R-SERS substrate. Sensitivity of SERS substrate directly affects detection limit of target molecules, which is vital to practical applications of pesticide resume detections. Frequently-used Raman probe R6G was applied to investigate the sensitivity of Ag@R-SERS substrate. Fig. 3(a) exhibits an intensity comparison of R6G (10^{-6} M) signals obtained from an Ag@R-SERS substrate (red line), Ag decorated flat polymer film (orange line). And Raman spectra obtained from a blank Ag@R-SERS substrate (green line) and flat polymer film (blue line). Fig. 3(b) demonstrates SERS spectrums of R6G with different concentrations obtained from Ag@R-SERS substrate and a reference Raman spectrum of R6G at the concentration of 10^{-1} M without any enhancement. The characteristic Raman peaks of R6G mainly locate at 611, 771, 1125, 1189, 1308, 1360, 1513, 1649 cm^{-1}. As the concentrations of R6G solution decrease, the Raman signals are weakened. There are still obvious R6G signals on Ag@R-SERS substrate as the concentration of R6G is low to 10^{-8} M (10 nM). The enhancement factor (EF) was calculated by formula (I), where I_{SERS}, I_{bulk} represent the SERS signal intensity and the bulk Raman signal intensity of probe with and without SERS substrate respectively, and N_{SERS}, N_{bulk} denote corresponding molecule numbers within the measurement regions. For the Ag@R-SERS substrate, the calculated EF was determined to be 5.9×10^7. It is noteworthy that a SERS enhancement factor on the order of 10^7 to 10^8 is sufficient to enable the observation of single-molecule.[25] Fig. 3(c) exhibits a linear relationship between the concentrations of R6G and the corresponding peak intensities at 1513 cm^{-1} over the range of 10^{-8} to 10^{-6} M. The linear correlation coefficient squared (R^2) is 0.9921. The limit of detection

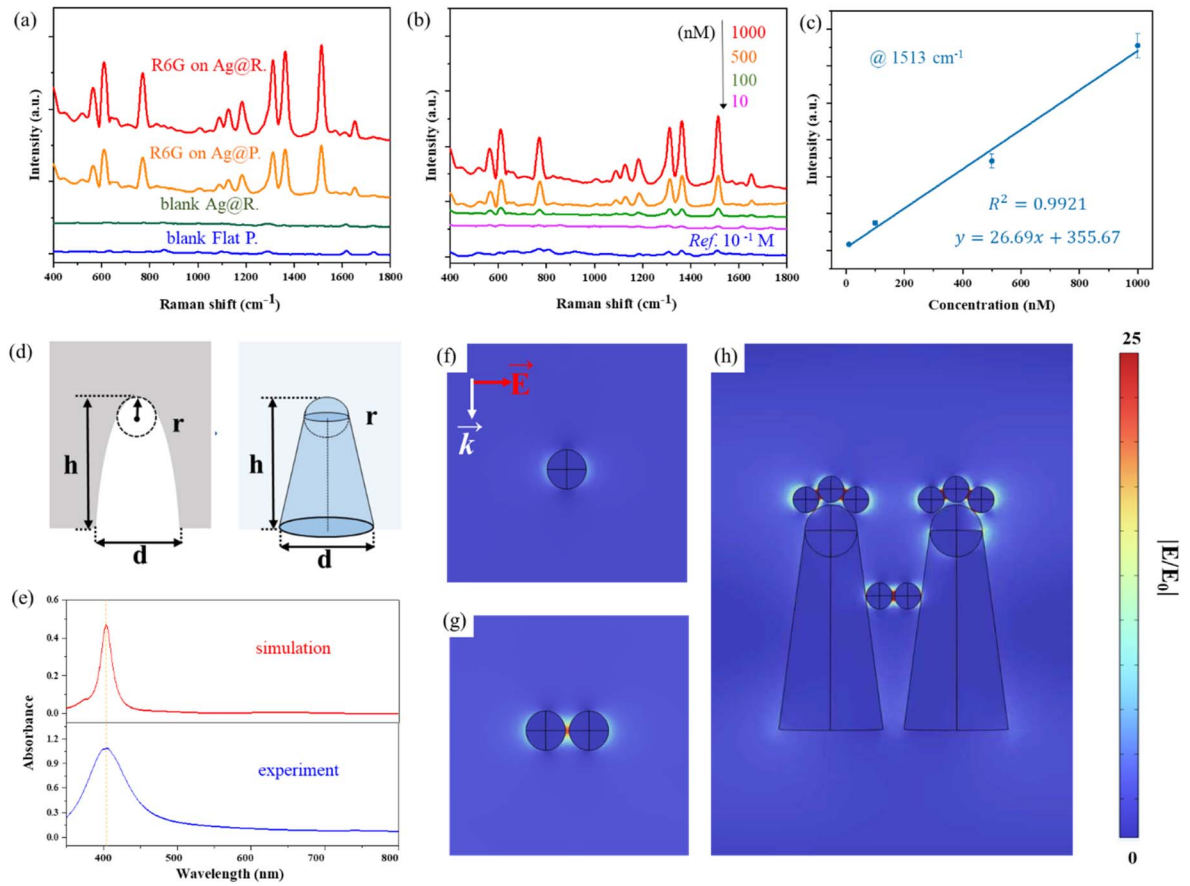

Fig. 3 (a) The Raman spectra of R6G obtained from an Ag@R-SERS substrate (red line), Ag decorated flat polymer film (orange line). The Raman spectra obtained from a blank Ag@R-SERS substrate (green line) and flat polymer film (blue line). (b) The Raman spectra of R6G with different concentrations obtained from Ag@R-SERS substrates and reference Raman spectra of R6G at the concentration of 10^{-1} M. (c) Linear relation of Raman intensities at 1513 cm^{-1} and concentrations of R6G. (d) Simplified structure and parameters of nano-cone. (e) Simulated and experimental UV-VIS spectrums of Ag NPs. (f) Simulated *E*-field distribution of silver single-particle model at 785 nm. (g) Simulated *E*-field distribution of silver two-particle model with a gap of 5 nm at 785 nm. (h) Simulated *E*-field distributions of Ag NPs on PET nano-cones. *E* is the polarisation direction and *k* is the propagation direction. The wavelength of the incident light is 785 nm.

(LOD) for R6G calculated using formula (II) is determined to be 2.65×10^{-8} M, where σ represents the standard deviation of the blank samples and k denotes the slope of the linear fitting line.[26,27]

$$\mathrm{EF} = \frac{I_{\mathrm{SERS}}/N_{\mathrm{SERS}}}{I_{\mathrm{bulk}}/N_{\mathrm{bulk}}} \quad \text{(I)}$$

$$\mathrm{LOD} = \frac{3\sigma}{k} \quad \text{(II)}$$

As indicated in Fig. 3(a), Raman signals of low concentration R6G were achieved benefitting from the attendances of noble metal nanoparticles. Meanwhile, the Ag NPs layer deposited on the polymer film reduces the intrinsic and interference signals of substrates to a great extent. The intensities of R6G detected on the Ag@R-SERS substrate are approximately six times higher than those obtained from the Ag NPs decorated polymer film. To estimate the increment of surface area with the existences of cone-shape nanostructures, the periodical nano-cone was simplified as a composition of a circular truncated cone and a hemisphere as shown in Fig. 3(c). The ratio of surface area (S_{I}) to projected area (S_{II}) of nano-cone is approximate to increment coefficient, where the S_{I} and S_{II} are calculated as formula (III) and (IV). All the parameters in the simplified model are in accordance with AAO mold schematically shown in Fig. 3(c). It is estimated that there is a four times areal enlargement benefitted from the nano-cone arrays, which provides more abundant supporting sites to load high-density Ag NPs. Moreover, the cone-shape nanostructured film has good hydrophobicity which might facilitate a high concentration of Ag NPs, and Ag NPs would be deposited on the based film with narrow gaps.

$$S_{\mathrm{I}} = \pi\left(\frac{d}{2}+r\right)\sqrt{\left(\frac{d}{2}-r\right)^2+(h-r)^2}+2\pi r^2 \quad \text{(III)}$$

$$S_{\mathrm{II}} = \pi\left(\frac{d}{2}\right)^2 \quad \text{(IV)}$$

From the perspective of the widely accepted electromagnetic mechanism, the intense localized electromagnetic fields (*E*-fields) generated by noble metal nanostructures under incident laser excitations are the primary contributors to the high sensing sensitivity of plasmonic SERS substrates. As illustrated in Fig. 3(f)–(h), *E*-field distribution of silver single-particle, two-particle simplified models and Ag NPs on PET nano-cones were constructed and analyzed by finite element method (FEM). The dielectric constant of silver was obtained from the Drude model, while the refractive index of vacuum was set to 1 and that of PET to 1.6, respectively. The radius of the nanosphere is set as 25 nm according to experimental UV-VIS spectra of diluent Ag NPs colloids in Fig. 3(e). As observed from the Fig. 3(e), the localized surface plasmon resonance (LSPR) of silver nanospheres occurs at approximately 410 nm and the silver nanosphere behaves as an electric dipole under the incident excitation, which generates a strong localized electric field enhancement parallel to the direction of electric polarization. As illustrated in Fig. 3(f), the electric field enhancement sharply declines as the wavelength of incident laser deviates from the LSPR peak. Nonetheless, as shown in Fig. 3(g), the coupling effect between adjacent silver nanospheres could also induce a considerable degree of localized electric field enhancement in the narrow gaps. The coupling enhancement effect formed by densely distributed silver nanoparticles is less sensitive to the wavelength of incident light than the LSPR effect of a single silver nanoparticle. The large specific surface areas and hydrophobicity of well-ordered cone-shape arrays on the R-substrate have facilitated the high-density deposition of Ag NPs, which further enhances the sensitivity of Ag@R-SERS substrate. To further investigate the electromagnetic enhancements on the Ag@R-SERS substrate, *E*-field distributions of Ag NPs on PET nano-cones were analysed and shown in Fig. 3(h). As Ag clusters deposited on the tips of the nano-cones, a localized electric field enhancement is induced, although it exhibits a lower intensity than the lightning-rod effect of sharp-tipped nanostructures composed entirely of noble metals.[28,29] Furthermore, intense electromagnetic coupling among Ag NPs loaded on neighboring nano-cones is observed in Fig. 3(h), and these effects jointly endow the SERS substrate with excellent sensitivity performances.

3.2.2 Uniformity, reproducibility, stability of Ag@R-SERS substrate. Uniformity, reproducibility, and stability of SERS substrate are of great importance for SERS substrate, which are closely related to the practicability and reliability of further applications. The relative standard deviations (RSDs) of characteristic Raman peaks are frequently-used index to evaluate site-to-site and batch-to-batch fluctuations of SERS substrates. The RSD could be calculated as formula (V) and (VI), where $\bar{X}$, SD, and n is respectively mean value, standard deviation of the characteristic Raman peak, and amount of Raman spectra.

Fig. 4(a) and (d) demonstrated SERS spectrums and corresponding peak intensities of R6G at 1513 cm^{-1} obtained from 10 random test points on one Ag@R-SERS substrate to evaluate the uniformity performances of Ag@R-SERS substrates. The calculated RSD is 5.6%. Fig. 4(b) and (e) were SERS spectra and corresponding peak intensities of R6G at 1513 cm^{-1} detected on Ag@R-SERS substrates from different batches ($n = 10$) to evaluate reproducibility performances. The calculated RSD is 6.7%. The RSDs less than 20% are generally regarded as acceptable results for SERS substrate.[30] The results of 5.6% and 6.7% detected and evaluated on Ag@R-SERS substrates demonstrated good uniformity and reproducibility. To mitigate the negative impacts of the ambient atmosphere and light exposure, the Ag@R-SERS substrates were vacuum-sealed in aluminum foil bags using a household vacuum sealer to extend their storage life. Fig. 4(c) were SERS spectra of R6G obtained from Ag@R-SERS substrate with different storage durations and Fig. 4(f) illustrated the corresponding peak intensities (green bars) of the characteristic peak at 1513 cm^{-1}. There were no obvious changes in the spectral profile of R6G detected on the SERS substrate stored for 20 days, whereas the intensity of the

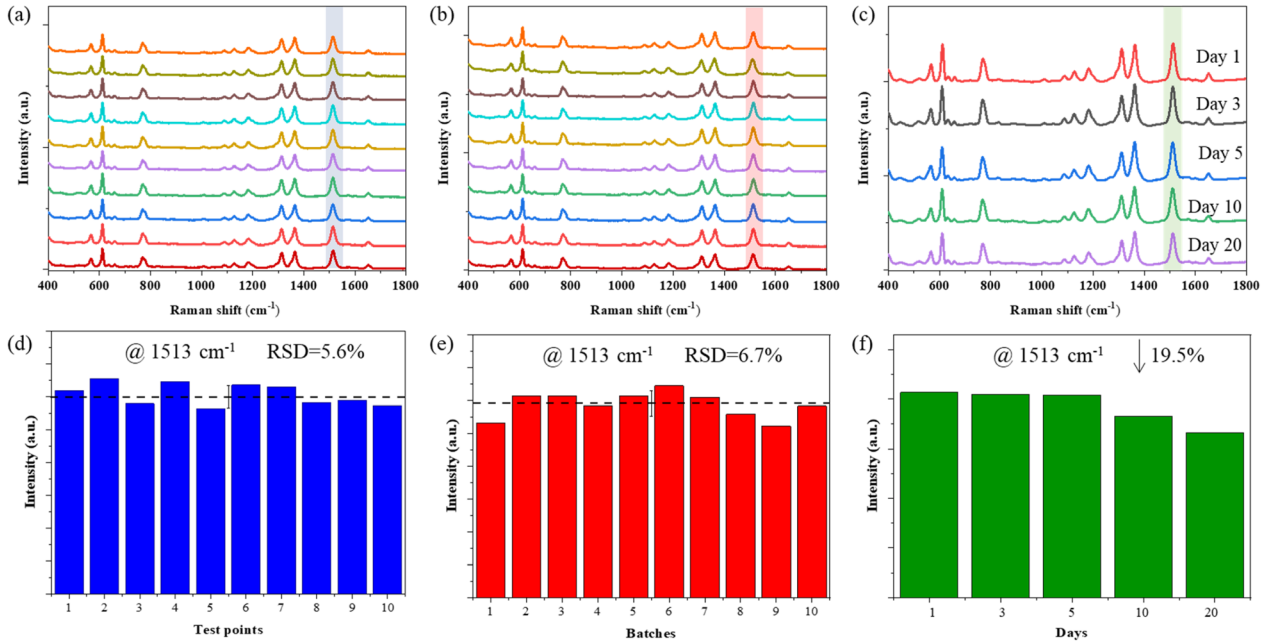

Fig. 4 (a) SERS spectra of R6G obtained from different test points on an Ag@R-SERS substrate ($n = 10$); (d) corresponding intensities (blue-bar), mean value (dash-line), and standard deviation (scale-bar) of characteristic peak at 1513 cm^{-1}. (b) SERS spectra of R6G detected on Ag@R-SERS substrates from different batches ($n = 10$); (e) corresponding intensities (red-bar), mean value (dash-line), and standard deviation (scale-bar) of characteristic peak at 1513 cm^{-1}. (c) SERS spectra of R6G obtained from Ag@R-SERS substrate with different storage days; (f) corresponding intensities (green-bar) of characteristic peak at 1513 cm^{-1}.

Raman characteristic peak at 1513 cm^{-1} underwent a 20% reduction.

The presence of cone-shaped nanostructures on the Ag@R-SERS substrate significantly increased surface area, provide abundant anchoring sites for the stable immobilization of Ag NPs which effectively inhibit aggregations of nanoparticles. The structural merits, combined with a reproducible fabrication process, contributed to satisfactory uniformity, reproducibility and shelf-life of Ag@R-SERS substrate.

$$\mathrm{RSD} = \frac{\mathrm{SD}}{\overline{X}} \times 100\% \quad \text{(V)}$$

$$\mathrm{SD} = \sqrt{\frac{\sum_{i=1}^{n}\left(x - \overline{X}\right)^2}{n}} \quad \text{(VI)}$$

3.3 Pesticide residue detection of Ag@R-SERS substrate

To further explore the potential of Ag@R-SERS substrate for pesticide detection, thiram was selected as a model analyte for detection and analysis. Thiram is a widely used fungicide that protects grains, seeds, vegetables, and fruits against fungal diseases. Although thiram exhibits low toxicity, it still poses health risks to humans and potential hazards to the environment. The U.S. Environmental Protection Agency (EPA) has set a tolerance limit of 7 ppm for thiram in fruits, while the Ministry of Agriculture of the People's Republic of China (P.R.C.) has prescribed a maximum residue limit (MRL) of 5 ppm for common fruits and vegetables.

Fig. 5(a)–(c) show the Raman spectra of thiram detected in ethanol solution, apple juice, and tomato juice matrices, respectively. It is evident that the dominant Raman peaks of thiram are located at 564, 938, 1148, 1386, and 1514 cm^{-1}, which can be assigned to the S–S stretching mode, C–S stretching mode, C–N stretching mode or CH_3 rocking mode, C–N stretching mode or CH_3 deformation mode, and C–N stretching mode, respectively.[17,18] As the concentration of thiram decreased, the intensity of the Raman peaks gradually weakened. Notably, distinct Raman signals were still detectable even when the thiram concentration was below the aforementioned tolerance limits. Fig. 5(d) illustrates the linear relationships between thiram concentration and Raman intensity at 1386 cm^{-1}. The analytical parameters of the linear models are summarized in Table 1. The coefficients of determination (R^2) of the models were 0.9986, 0.9940, 0.9974, and the estimated LODs calculated by formula (II) were 0.46, 0.49, 0.55 ppm in ethanol solution, apple juice and tomato juice, respectively. A detailed comparison of reported SERS substrates, including their substrate properties, set-up types, and lowest detectable concentration or LOD, is provided in Table S1 in the SI. The Ag@R-SERS substrate coupled with the Hx-Spec delivers performance competitive with that of previously reported substrates integrated with commercial portable Raman spectrometers or bench-top setups.[31–37] Sensitive thiram detection further verifies the high sensitivity of the Ag@R-SERS substrate. And Fig. S2 demonstrates 10 times random detections of

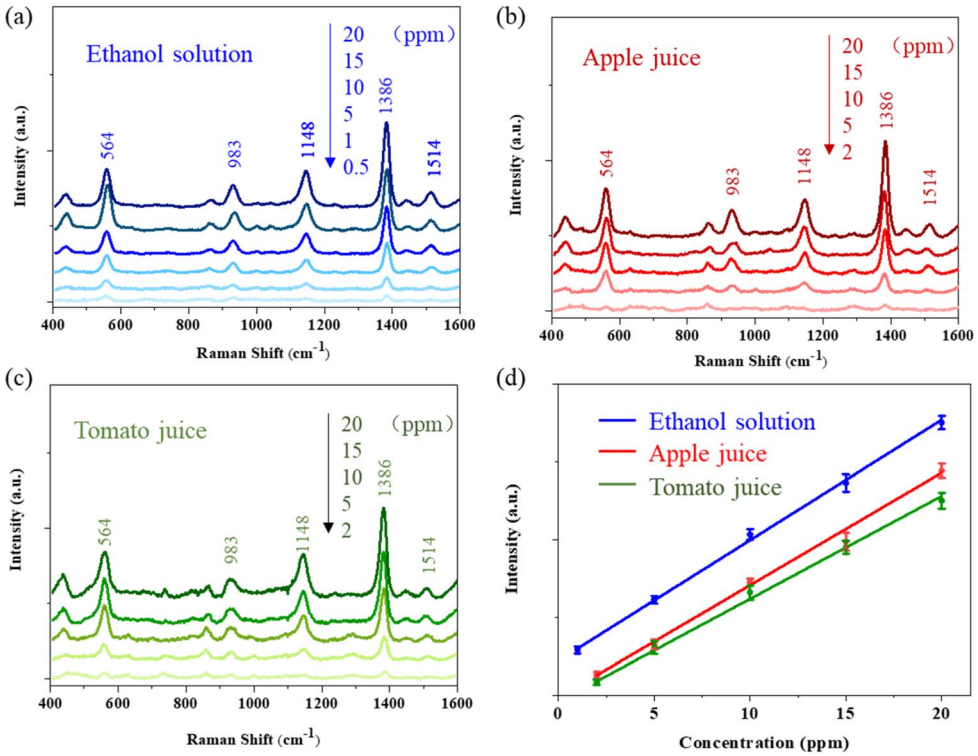

Fig. 5 The Raman spectra of thiram in (a) ethanol solution; (b) apple juice; and (c) tomato juice detected on Ag@R-SERS substrates. (d) Linear relations of thiram concentrations and Raman intensities at 1386 cm^{-1}.

Table 1 Analytical results of the model

Matrix	Slope	Intercept	*R*-Square	LOD (ppm)
Ethanol	1529	458	0.9986	0.46
Apple juice	1431	−471	0.9940	0.49
Tomato juice	1292	−452	0.9974	0.55

thiram. The corresponding RSD of characteristic peak at 1386 cm^{-1} is 6.3%, which is comparable to the values evaluated by R6G. It confirms the reproducibility performances of Ag@R-SERS substrate for thiram detections. These experimental results demonstrate that Ag@R-SERS substrate exhibits potential for practical application in the sensitive and rapid detection of pesticide residues.

4. Conclusions

In summary, a two-step approach for fabricating large-scale, flexible Ag@R-SERS substrates was developed, and their applicability in pesticide detection was investigated. The active surface area is significantly increased by the highly-ordered nano-cones fabricated by the roll-to-roll UV-nanoimprint lithography technique, which provide abundant anchoring sites for silver nanoparticles. The electromagnetic enhancement effects of Ag@R-SERS substrates were investigated *via* finite element method models. The enhancement effects might be jointly attributed to strong coupling effects of densely distributed AgNPs and Ag clusters at the tips of nano-cone. Using a portable Raman spectrometer, the EF and LOD of R6G on the flexible Ag@R-SERS substrate was determined to be 5.9×10^{7} and 2.65×10^{-8} M, respectively. The relative standard deviations (RSDs) of R6G Raman intensities at 1513 cm^{-1} were 5.6% on a single Ag@R-SERS substrate and 6.7% across different substrates. There were no obvious changes observed in the line curve of R6G detected on the SERS substrate stored for 20 days, and the signal intensity of its characteristic peak only attenuated by 20%. These results indicated satisfactory sensitivity, uniformity, reproducibility, stability of the Ag@R-SERS substrate, which were critical for practical SERS applications. Furthermore, the feasibility of the Ag@R-SERS substrate for pesticide detection was demonstrated taking thiram as a model analyte. A good linear relationship was established between the thiram concentration and Raman intensity at 1386 cm^{-1} with R^2 of 0.9986, 0.9940, 0.9974 and LOD of thiram was determined to be 0.46, 0.49 and 0.55 ppm in ethanol, apple juice and tomato juice, respectively. These results experimentally illustrated that the Ag@R-SERS substrate coupled with a portable spectrometer Hx-Spec enabled near-single-molecule level detection and compliance screening of pesticide residue with good performances of uniformity, reproducibility, stability. In future work, the sensitivity of the Ag@R-SERS substrate could be further enhanced by regulating the density of silver nanoparticle distribution and introducing nanostructures that generate strong intrinsic electromagnetic hotspots. Moreover, analytical performance of Ag@R-SERS substrate for other pesticides and

illegal additives in agricultural products would be further investigated.

Author contributions

Jie Chen: conceptualization, methodology, investigation, data curation, writing – original draft, funding acquisition. Mengjie Hu: investigation, data curation, visualization. Tianyuan Liu: formal analysis, writing – review and editing. Meizhen Huang: conceptualization, supervision, writing – review and editing. Lili Kong: validation, formal analysis, writing – review and editing. Xinna Yu: data curation, visualization, writing – review and editing. Qifang Sun: conceptualization, validation, writing – review and editing.

Conflicts of interest

There are no conflicts to declare.

Data availability

The data that support the findings of this study are available from the corresponding author upon reasonable request.

Supplementary information (SI) is available. See DOI: https://doi.org/10.1039/d6ra00131a.

Acknowledgements

This work was supported by the National Natural Science Foundation of China (No. 62105207, 62175150, 62305211).

Notes and references

1 R. Wen, Y. Han, X. Tang, *et al.*, *Trends Food Sci. Technol.*, 2025, **160**, 104995.
2 J. Neng, J. Wang, Y. Wang, *et al.*, *Food Chem.*, 2023, **429**, 136883.
3 M. Yan, H. Li, M. Li, *et al.*, *J. Agric. Food Chem.*, 2021, **69**, 14049–14064.
4 H. Zhao, C. Chen, Y. Wang, *et al.*, *Spectrochim. Acta, Part A*, 2025, **330**, 125731.
5 X. Yu, L. Kong, T. Lan, *et al.*, *Spectrochim. Acta, Part A*, 2025, **328**, 125429.
6 L. Kong, J. Chen and M. Huang, *Sens. Actuators, B*, 2021, **344**, 130163.
7 X. Yu, T. Lan, L. Kong, *et al.*, *Surf. Interfaces*, 2024, **44**, 103763.
8 T. Liu, J. Chen, L. Kong, *et al.*, *Food Biosci.*, 2024, **57**, 103465.
9 Q.-D. Mai, D. T. H. Trang, N. T. Loan, *et al.*, *RSC Adv.*, 2024, **14**, 36960–36969.
10 R. Wang and J. Luo, *RSC Adv.*, 2023, **13**, 499–505.
11 A. S. Rourke-Funderburg, A. B. Walter, B. Carroll, *et al.*, *ACS Omega*, 2023, **8**, 33745–33754.
12 N. C. Martins, S. Fateixa, H. I. Nogueira, *et al.*, *Analyst*, 2024, **149**, 244–253.
13 T. Ma, X. Dong, I. Liang, *et al.*, *Talanta*, 2025, **294**, 128170.
14 S. Han, C. Zhang, S. Lin, *et al.*, *Spectrochim. Acta, Part A*, 2021, **251**, 119463.
15 T. K. Naqvi, A. Bajpa, S. Dwivedi, *et al.*, *Sens. Actuators, A*, 2023, **356**, 114341.
16 R. Chen, Y. Qu, Z. Ma, *et al.*, *Cellulose*, 2024, **31**, 11.
17 Z. Xiong, M. Lin, H. Lin, *et al.*, *Carbohydr. Polym.*, 2018, **189**, 79–86.
18 J. Chen, M. Huang, L. Kong, *et al.*, *Carbohydr. Polym.*, 2019, **205**, 596–600.
19 G. Weng, Y. Feng, J. Zhao, *et al.*, *Sens. Actuators, B*, 2020, **308**, 127754.
20 C. Jiao, X. Liang, X. Wu, *et al.*, *Anal. Chem.*, 2024, **96**, 13042–13049.
21 H. Wang, C. Wang, Q. Nie, *et al.*, *Chem. Eng. J.*, 2024, **490**, 151565.
22 L. Li, J. Zhao, S. Wu, *et al.*, *Opt. Express*, 2025, **33**, 12989.
23 C. Zhang, P. Yi, L. Peng, *et al.*, *Sci. Rep.*, 2017, **7**, 39814.
24 N. Leopold and B. Lendl, *J. Phys. Chem. B*, 2003, **107**, 5723.
25 M. Chen, R. Solarska and M. Li, *J. Phys. Chem. C*, 2023, **127**, 2728–2734.
26 Y. Zhou, A. Marar, P. Kner, *et al.*, *Anal. Chem.*, 2017, **89**, 5734–5741.
27 C. Zhu, G. Meng, P. Zheng, *et al.*, *Adv. Mater.*, 2016, **28**, 4871.
28 C. Zhu, G. Meng, P. Zheng, *et al.*, *Nanoscale*, 2012, **4**, 2663.
29 Y. Chen, W. Chang, C. Lee, *et al.*, *J. Mater. Chem. B*, 2022, **10**, 9974–9983.
30 P. P. Zhang, J. Gao and X. H. Sun, *Appl. Phys. Lett.*, 2015, **106**, 043103.
31 X. He, S. Yang S, T. Xu, *et al.*, *Biosens. Bioelectron.*, 2020, **152**, 112013.
32 Z. Wang, L. Zhang and Y. Chen, *Food Chem.: X*, 2023, **18**, 100670.
33 S. Lin, W. Hasi, S. Han, *et al.*, *Anal. Methods*, 2020, **12**, 2571.
34 L. Xiao, S. Feng, M. Z. Hua, *et al.*, *Talanta*, 2023, **254**, 124128.
35 V. Horváth, D. Megyeri, J. Kopniczky, *et al.*, *ACS Appl. Nano Mater.*, 2025, **8**, 17934–17951.
36 H. Sun, H. Liu and Y. Wu, *Appl. Surf. Sci.*, 2017, **416**, 704–709.
37 T. Wang, S. Zhang, D. Wu, *et al.*, *Microchem. J.*, 2025, **209**, 112656.